



## Determination of spin chirality using x-ray magnetic circular dichroism

Gerrit van der Laan 

*Diamond Light Source, Harwell Science and Innovation Campus, Didcot, Oxfordshire OX11 0DE, United Kingdom*

 (Received 11 June 2021; revised 20 August 2021; accepted 23 August 2021; published 9 September 2021)

A threefold symmetric kagome lattice that has negative spin chirality can give a nonzero x-ray magnetic circular dichroism (XMCD) signal, despite the total spin moment amounting to zero. In order to explain this, I present here a rule for the rotational symmetry invariance of the XMCD signal. A necessary condition is the existence of an anisotropic XMCD signal for the local magnetic atom, which can arise from a spin anisotropy either in the ground state or the final state. The angular dependence of the XMCD as a function of the beam direction has an unusual behavior. The maximum dichroism is not aligned along the spin direction, but depends on the relative orientation of the spin with respect to the atomic orientation. Therefore, different geometries can result in the same angular dependence, and the spin direction can only be determined if the atomic orientation is known. The consequences for the x-ray magneto-optical sum rules are given. The integrated XMCD signals are proportional to the anisotropy in the orbital moment and the magnetic dipole term, where the isotropic spin moment drops out.

DOI: [10.1103/PhysRevB.104.094414](https://doi.org/10.1103/PhysRevB.104.094414)

### I. INTRODUCTION

X-ray magnetic circular dichroism (XMCD) has become a versatile technique to interrogate ferro- and ferrimagnetic magnetic materials [1]. Particularly huge XMCD signals are observed in the soft x-ray region [2], facilitating us to extract the expectation values of the element-specific spin and orbital moments [3,4]. On the other hand, common wisdom has it that there is no XMCD from antiferromagnetic (AFM) materials, where the spin moments for the particular element cancel each other [5].

Recently, Yamasaki *et al.* [6] conjectured the existence of XMCD in the coplanar  $120^\circ$  AFM kagome network of  $\text{Mn}_3\text{Sn}$ . These authors ascribed the origin of the XMCD to the magnetic dipole term  $\langle T_z \rangle$ . This term gives the anisotropy of the spin distribution [4] and is contributing to the magnetocrystalline anisotropy energy [7]. Subsequently, Sasabe *et al.* [8] performed cluster calculations for the XMCD at the  $L_{2,3}$  absorption edge of  $\text{Fe}^{2+} d^6$  in a kagome lattice, thereby theoretically confirming the presence of XMCD. However, they also found XMCD for  $\text{Mn}^{2+} d^5$  in a kagome lattice, which has a negligibly small  $\langle T_z \rangle$ , thereby dismissing it as the origin of the effect.

Also the spin-polarized relativistic (SPR) Korringa-Kohn-Rostoker (KKR) calculations for  $\text{Mn}_3\text{Ir}$  and  $\text{Mn}_3\text{Ge}$  by Wimmer *et al.* [9] confirmed a nonzero XMCD. It has been suggested that this is connected to a chirality-driven orbital magnetic moment [10]. The scalar spin chirality is closely

related to the emergent magnetic field, a natural concept in the geometric theories of the Hall effect and orbital magnetization [11]. It however requires a noncoplanar rather than a non-collinear magnetic structure [12]. In noncoplanar structures, the anomalous Hall effect (AHE) has been associated through the Berry phase with spin chirality [13–16]. For diluted magnetic systems it was shown that if three spins  $S_0$ ,  $S_1$ , and  $S_2$  are noncoplanar, they contribute to the AHE with a term which is proportional to the scalar chirality  $S_0 \cdot (S_1 \times S_2)$  [14]. This mechanism for AHE does not involve a spin-orbit interaction, but requires only the existence of noncoplanar (chiral) spin configurations.

The structure of a two-dimensional (2D) kagome lattice with threefold symmetry axes is displayed in Fig. 1. The dashed box marks a unit cell of the magnetic structure. In the spin-oriented state the red, blue, and green atoms have different spin directions. With the spin of each atom rotated by  $120^\circ$ , the AFM structure has no net spin moment. Naively,

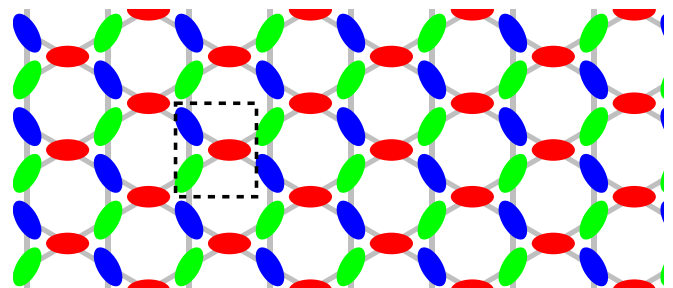


FIG. 1. Structure of two-dimensional kagome lattice with threefold symmetry axes and corner-sharing triangles. Only the magnetic atoms are shown. In the spin-oriented state the red, blue, and yellow atoms have different spin directions. The dashed box indicates a unit cell of the magnetic structure.

one might then expect a zero XMCD, as is indeed so if the structure has positive chirality (defined as spin and atomic orientation having the same sense of rotation). However, this is not necessarily true for negative helicity (defined as spin and atomic orientation having opposite sense of rotation). As a relevant example,  $\text{Mn}_3\text{S}$  is a hexagonal AFM with space group  $P6_3/mmc$  [17]. Below the Néel temperature  $T_N \approx 430$  K, the combination of intersite AFM and Dzyaloshinskii-Moriya interactions leads to a  $120^\circ$  spin structure with a uniform negative spin chirality of the in-plane Mn moments because of geometrical frustration. It exhibits a large anomalous Hall conductivity [18] and magneto-optic Kerr effect (MOKE) [19] despite the absence of a net magnetic moment.

From the viewpoint of XMCD several questions remain to be addressed: What is the origin of the nonzero XMCD in the threefold symmetric AFM structure? Is this effect also present for other  $n$ -fold AFM structures, notably skyrmions? Can the XMCD be used to deduce the spin direction? What roles are played by the orbital moment and the magnetic dipole term of the atoms? These questions will be answered in the following.

## II. OCCURRENCE OF XMCD

### A. Angular dependence

In x-ray absorption spectroscopy (XAS) at the  $L_{2,3}$  edge of a  $3d$  transition metal a  $2p$  core electron is excited into an unoccupied  $3d$  state. The participation of the core hole makes that the excitation process is localized, i.e., restricted to the excited atom in the ligand field of the neighboring atoms. The XMCD is obtained as the difference between two XAS spectra with opposite light helicities.

A general description of the angular dependence of the XMCD in three dimensions can be found elsewhere [20,21], but as the minimal model to study the coplanar case two dimensions are sufficient. For an isotropic system the XMCD signal is proportional to  $\hat{\mathbf{P}} \cdot \hat{\mathbf{S}}$ , where  $\hat{\mathbf{P}}$  is the light helicity vector, which is always along the beam direction, and  $\hat{\mathbf{S}}$  is the spin vector. In a lower than octahedral environment of the atom the XMCD will be anisotropic with respect to the atomic axes. With the spin  $\hat{\mathbf{S}}$  in the  $x$ - $y$  plane the XMCD spectrum can then be written as

$$I_{\text{XMCD}} = I_x(\hat{\mathbf{P}} \cdot \hat{\mathbf{x}})(\hat{\mathbf{x}} \cdot \hat{\mathbf{S}}) + I_y(\hat{\mathbf{P}} \cdot \hat{\mathbf{y}})(\hat{\mathbf{y}} \cdot \hat{\mathbf{S}}), \quad (1)$$

where  $I_x$  and  $I_y$  are the energy-dependent XMCD signals for  $\hat{\mathbf{P}} \parallel \hat{\mathbf{S}}$  along the local  $\hat{\mathbf{x}}$  and  $\hat{\mathbf{y}}$  directions of the excited atom, respectively. The intensity  $I \equiv I(E)$  is at an arbitrary photon energy.

The intensity of each peak in the XMCD multiplet can have a different angular dependence. Equation (1) accounts for this by using a linear combination of so-called fundamental spectra. For electric-dipole transitions in a 2D system there can be only two fundamental spectra, which we take as  $I_x(E)$  and  $I_y(E)$  (for electric-quadrupole transitions there would be more than two spectra). Specifically, the ratio  $I_x/I_y$  will change as a function of photon energy  $E$ . An example of the angular dependence of the XMCD in uniaxial symmetry described by two fundamental spectra can be found in Ref. [21].

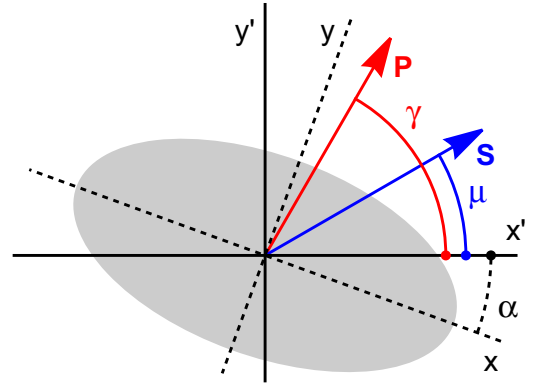


FIG. 2. Definition of the angles in the reference frame. The local atom (gray disk) is oriented along  $x$ , which makes an angle  $\alpha$  with the  $x'$  axis of the laboratory frame. The spin direction  $\hat{\mathbf{S}}$  and the helicity vector  $\hat{\mathbf{P}}$  of the circularly polarized x rays are at an angle  $\mu$  and  $\gamma$ , respectively, with respect to  $x'$ .

With the beam direction fixed, each individual atom  $k$  in the kagome unit cell has a different orbital orientation and spin direction. It is assumed that in the local frame each atom has the same absorption coefficient. The atom  $k$  is oriented along the local  $x$  axis, which makes an angle  $\alpha_k$  with the laboratory axis  $x'$ , so that Eq. (1) can be recast as

$$I_{\text{XMCD}}^k = I_x \cos(\gamma - \alpha_k) \cos(\mu_k - \alpha_k) + I_y \sin(\gamma - \alpha_k) \sin(\mu_k - \alpha_k), \quad (2)$$

where  $\gamma$  and  $\mu_k$  are the angles of  $\hat{\mathbf{P}}$  and  $\hat{\mathbf{S}}$ , respectively, with respect to  $x'$  (see Fig. 2). Indeed, Eq. (2) obeys the correct symmetry properties

$$\begin{aligned} I_{\text{XMCD}}^k(\gamma + \pi) &= -I_{\text{XMCD}}^k(\gamma), \\ I_{\text{XMCD}}^k(\mu_k + \pi) &= -I_{\text{XMCD}}^k(\mu_k), \\ I_{\text{XMCD}}^k(\alpha_k + \pi) &= +I_{\text{XMCD}}^k(\alpha_k), \end{aligned}$$

for reversal of the light direction, spin direction, and atomic orientation, respectively.

In the absence of anisotropy ( $I_x = I_y$ ), Eq. (2) reduces to  $I_{\text{XMCD}}^k = I_x \cos(\gamma - \mu_k)$ , which summed over  $k$  for an AFM lattice yields a net zero XMCD. Thus, it can already be stated that some form of anisotropy would be a necessary condition to have a nonzero total XMCD.

The magnetic unit cell of the kagome lattice, shown in Fig. 1, can have different spin chiralities as depicted in Fig. 3. Starting from the  $x'$  axis, the three atoms and their spins, with angles  $\alpha_k$  and  $\mu_k$ , are labeled  $k = 0, 1, 2$  in the counterclockwise convention, and colored red, blue, and green, respectively. Taking  $\alpha_0 = 0^\circ$ , examples are shown with  $\mu_0 = 0^\circ, 20^\circ, \text{ and } 90^\circ$ . In the case that  $\alpha_0 \neq 0^\circ$  we are free to rotate the unit cell to  $\alpha_0 = 0^\circ$ , i.e., align along the  $x'$  axis. For positive chirality ( $h = 1$ ) the atomic orientation and spin direction in Fig. 3 follow the same sense of rotation, increasing by  $120^\circ$  between the respective atoms in the triangle. In contrast, for negative chirality ( $h = -1$ ) the spin direction has the opposite sense of rotation as the atomic orientation.

For positive chirality, the threefold rotational symmetry of the structure leads to a vanishing total XMCD. For, e.g.,

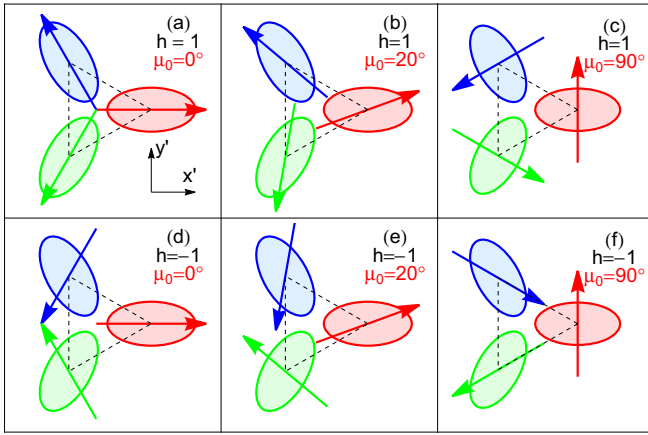


FIG. 3. Magnetic unit cells oriented along  $\alpha_0 = 0^\circ$  with positive chirality ( $h = 1$ ) for (a)  $\mu_0 = 0^\circ$  ( $A_2$  phase), (b)  $\mu_0 = 20^\circ$ , and (c)  $\mu_0 = 90^\circ$  ( $A_1$  phase), and with negative chirality ( $h = -1$ ) for (d)  $\mu_0 = 0^\circ$ , (e)  $\mu_0 = 20^\circ$ , and (f)  $\mu_0 = 90^\circ$ .

Figs. 3(a) and 3(c), Eq. (2) gives for the atom  $k$ ,

$$\begin{aligned} I_{\text{XMCD}}^k &= I_x \cos(\gamma - \alpha_k) \quad \text{for } \mu_k = \alpha_k, \\ I_{\text{XMCD}}^k &= I_y \sin(\gamma - \alpha_k) \quad \text{for } \mu_k = \alpha_k + 90^\circ, \end{aligned} \quad (3)$$

respectively. Since  $\gamma$  is fixed with respect to  $x'$  whereas  $\alpha_k$  is summed over  $k$ , the total XMCD amounts to zero. However, for negative chirality the combination of atomic orientation and spin direction lacks rotational symmetry. For completeness the symmetry properties of the spin vectors are given in the Appendix, although no explicit use will be made of group-theoretical arguments. Instead a more transparent analytical derivation is given.

### B. General derivation

Equation (2) can be recast into a sum over an isotropic and an anisotropic part as

$$\begin{aligned} I_{\text{XMCD}}^k &= \frac{1}{2}(I_x + I_y) \cos(\gamma - \mu_k) \\ &+ \frac{1}{2}(I_x - I_y) \cos(\gamma + \mu_k - 2\alpha_k). \end{aligned} \quad (4)$$

Both chiralities can be captured by taking the angles for atom  $k$  as

$$\begin{aligned} \alpha_k &= \alpha_0 + \frac{2\pi}{3}k, \\ \mu_k &= \mu_0 + \frac{2\pi}{3}kh, \end{aligned} \quad (5)$$

where  $h = +1$  and  $-1$  for positive and negative chirality, respectively. This gives

$$\begin{aligned} I_{\text{XMCD}}^k &= \frac{1}{2}(I_x + I_y) \cos\left(\gamma - \mu_0 - \frac{2\pi}{3}kh\right) \\ &+ \frac{1}{2}(I_x - I_y) \cos\left[\gamma + \mu_0 - 2\alpha_0 + \frac{2\pi}{3}k(h-2)\right]. \end{aligned} \quad (6)$$

Summing over  $k = 0, 1, 2$  yields our key result, the total XMCD over the unit cell,

$$\begin{aligned} I_{\text{XMCD}}^{\text{total}} &= 0 \quad \text{for } h = +1, \\ I_{\text{XMCD}}^{\text{total}} &= \frac{3}{2}(I_x - I_y) \cos(\gamma + \mu_0 - 2\alpha_0) \quad \text{for } h = -1, \end{aligned} \quad (7)$$

where  $\gamma$ ,  $\mu_0$ , and  $\alpha_0$  have fixed values in the laboratory frame. Not surprisingly, the isotropic part has dropped out.

It can be immediately verified from Eq. (7) that if  $\alpha_0$  and  $\mu_0$  are increased by  $120^\circ$  and  $-120^\circ$ , respectively, then the intensity remains unchanged. Therefore, the anisotropic part for each of the three atoms is the same, so that the total XMCD is  $3 \times$  the individual atom contribution.

Equation (7) shows that for negative chirality the total XMCD does not vanish unless the XMCD of the local atom is isotropic ( $I_x = I_y$ ) or when  $\gamma = 2\alpha_0 - \mu_0 \pm 90^\circ$ , which corresponds to the zero crossings between positive and negative dichroism.

Further insight can be gained from a graphical illustration of the angular dependence of the XMCD as a function of the incident beam angle  $\gamma$ . Choosing for convenience  $I_x > I_y$  in Eq. (6), Fig. 4 shows angular plots with the lattice oriented at  $\alpha_0 = 0^\circ$ . The red, blue, and green curves give the XMCD for each of the three magnetic atoms with spin directions shown by the color-coded arrows. The corresponding magnetic unit cell is shown in the inset on the left.

Figure 4(a) shows a unit cell with positive helicity ( $h = 1$ ) and  $\mu_0 = 20^\circ$ . It demonstrates the threefold rotational symmetry of the angular dependence, whereby the total XMCD vanishes.

Figure 4(b) shows a unit cell with negative helicity and  $\mu_0 = 0^\circ$ . Here, the magnitude of the XMCD for the red atom is larger than that for the blue and green atoms, which is due to their different value for the angle  $|\mu_k - \alpha_k|$ . The total XMCD is shown by the thick black curve, and since  $\alpha_0 = \mu_0 = 0^\circ$  this gives  $I_{\text{XMCD}}^{\text{total}} = \frac{3}{2}(I_x - I_y) \cos \gamma$ , which has a maximum at  $\gamma = 0^\circ$ .

It becomes interesting when  $\mu_0 \neq 0$ , in which case the maximum dichroism is no longer oriented along  $S_0$  (the red arrow) since  $\gamma = -\mu_0$ . Figure 4(c) shows a unit cell with  $\mu_0 = 90^\circ$ . The magnitude of the XMCD for the red atom is smaller than that for the blue and green ones. The total XMCD is  $I_{\text{XMCD}}^{\text{total}} = -\frac{3}{2}(I_x - I_y) \sin \gamma$  with the maximum at  $\gamma = -90^\circ$ .

Both examples in Figs. 4(b) and 4(c) are consistent with the cluster calculations for the  $L_{2,3}$  XMCD of  $\text{Fe}^{2+} d^6$  and  $\text{Mn}^{2+} d^5$  in a kagome lattice, which were carried out by Sasabe *et al.* [8] using a fixed geometry.

Finally, Fig. 5 for  $h = -1$  and  $\mu_0 = 20^\circ$  reveals the intricacies of the anisotropy in the XMCD signal. For each of the atoms the angular dependence of the XMCD, shown in Fig. 5(a), is separated into its isotropic and anisotropic part. The isotropic part in Fig. 5(b) shows a threefold rotational symmetry and thus has no total XMCD. In the anisotropic part shown in Fig. 5(c), all three atoms give the same angular-dependent intensity, which is shown by the brown curve, and together these add up to the black curve. The total XMCD is  $\frac{3}{2}(I_x - I_y) \cos(\gamma + 20^\circ)$ , with a maximum at  $\gamma = -\mu_0 = -20^\circ$ , thus at the opposite site of the  $x'$  axis than  $S_0$ .

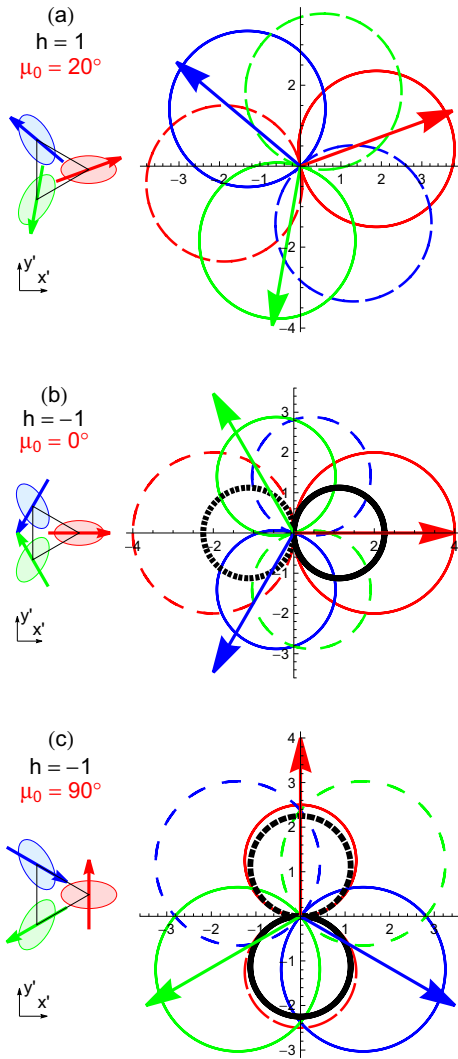


FIG. 4. The magnetic unit cell, oriented at  $\alpha_0 = 0^\circ$ , is shown in the inset at the left. The main image shows the angular dependence of the XMCD as a function of  $\gamma$ . The red, blue, and green curves give the XMCD for the three magnetic atoms with their spin directions shown by the color-coded arrows. The total XMCD is given by the thick black curve. The plots have been obtained from Eq. (6) for  $I_x = 4$ ,  $I_y = 2.5$ , and the solid and dashed curves correspond to positive and negative signals, respectively. (a) Positive helicity ( $h = 1$ ) with  $\mu_0 = 20^\circ$ , which gives a total XMCD = 0. (b) Negative helicity ( $h = -1$ ) with  $\mu_0 = 0^\circ$ , which gives a total XMCD =  $\frac{3}{2}(I_x - I_y)\cos\gamma$ , with maximum at  $\gamma = -\mu_0 = 0^\circ$ , i.e., along  $+x'$ . (c) Negative helicity with  $\mu_0 = 90^\circ$ , which gives a total XMCD =  $-\frac{3}{2}(I_x - I_y)\sin\gamma$ , with maximum at  $\gamma = -\mu_0 = -90^\circ$ , i.e., along  $-y'$ .

For a nonaligned lattice orientation ( $\alpha_0 \neq 0^\circ$ ), the maximum of the dichroism is found at  $\gamma = 2\alpha_0 - \mu_0$ . In the experiment, one can only determine the spin direction within this constraint, whereby different geometries can result in the same angular dependence. For instance, rotating the  $x'$  axis by  $90^\circ$  in Fig. 4(c) so that  $\alpha_0 = 90^\circ$  and  $\mu_0 = 180^\circ$  or rotating the  $x'$  axis by  $20^\circ$  in Fig. 5(a) so that  $\alpha_0 = 20^\circ$  and  $\mu_0 = 40^\circ$  gives in both cases exactly the same angular dependence as in Fig. 4(b) for  $\alpha_0 = \mu_0 = 0^\circ$ .

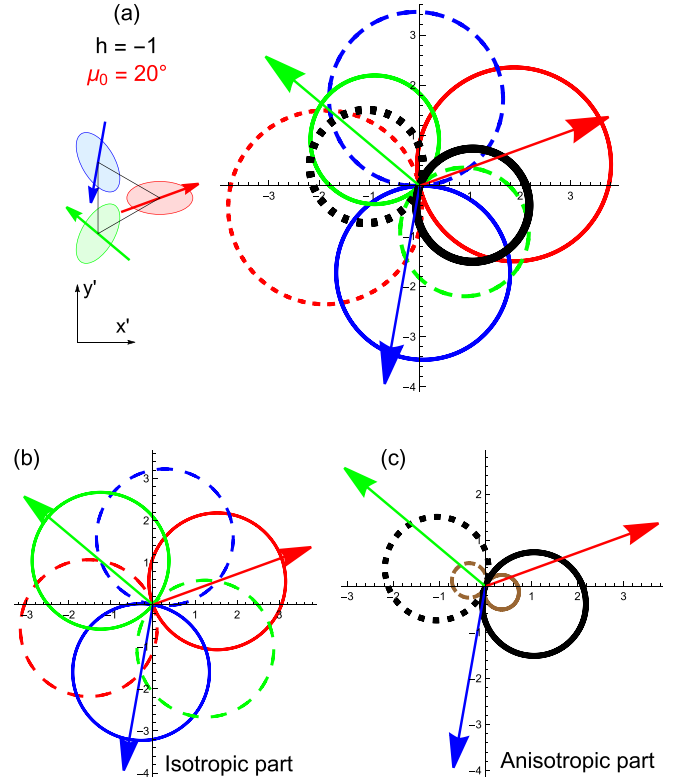


FIG. 5. (a) The angular dependence as a function of  $\gamma$  for negative helicity with  $\mu_0 = 20^\circ$ . The description of the plot is as in Fig. 4. The total XMCD =  $\frac{3}{2}(I_x - I_y)\cos(\gamma + 20^\circ)$ , which has a maximum for  $\gamma = -\mu_0 = -20^\circ$ , thus at the opposite site of the  $x'$  axis than  $S_0$  (red arrow). The lower panel shows the decomposition of the XMCD in isotropic and anisotropic part. (b) The isotropic part of the XMCD, which shows no total signal. (c) The anisotropic part, where all three magnetic atoms have the same angular dependence, shown by the brown curve, and which together add up to the black curve.

Hence, the angular dependent intensity as a function of the beam direction can be used to obtain the spin direction as long as the atomic orientation is known. Note that this also means that in the experiment particular care should be taken with the azimuthal alignment of the sample.

### C. Unit cell with multifold axis

Next, we consider whether a unit cell with  $n$ -fold rotational symmetry,  $C_{nv}$  ( $n \geq 2$ ), can have a nonvanishing total XMCD. Replacing  $\frac{2\pi}{3}$  by  $\frac{2\pi}{n}$  in Eq. (6) and summing  $k$  from 0 to  $n - 1$  gives that  $I_{\text{XMCD}}^{\text{tot}} = 0$  except for the above-treated case of ( $n = 3$ ,  $h = -1$ ). This also applies to  $n = 6$ , which can be considered as the sum of two lattices with  $n = 3$  that are rotated  $60^\circ$  with respect to each other. According to Eq. (7) the XMCD of these two unit cells have opposite signs and thus cancel each other out.

Skyrmions in crystalline lattices of B20-type compounds have sixfold symmetry axes and skyrmions in metallic multilayers might be regarded as having ( $n \rightarrow \infty$ )-fold symmetry, so that none of these will qualify for any total XMCD. However, resonant elastic x-ray scattering (REXS) has shown to be able to unambiguously resolve the chirality, owing to the interference effects between the different sites [22].

### III. SPIN AND ORBITAL GROUND STATE MOMENTS

#### A. Orbital moment

According to the orbital magnetic sum rule the expectation value of the ground state orbital moment  $\langle L_\zeta \rangle$  is proportional to the energy-integrated XMCD signal along the  $\zeta$  direction [3,23]. For the atom  $k$  the angular dependence is

$$\begin{aligned} \langle L^k \rangle &= \frac{1}{2}[\langle L_x \rangle + \langle L_y \rangle] \cos(\gamma - \mu_k) \\ &+ \frac{1}{2}[\langle L_x \rangle - \langle L_y \rangle] \cos(\gamma + \mu_k - 2\alpha_k), \end{aligned} \quad (8)$$

which agrees with Eq. (35) of Ref. [20]. Since this has the same angular dependence as the XMCD signal in Eq. (4), it can only be nonzero for a threefold lattice with negative chirality. Summation over  $k$  gives the total angular dependence for  $h = -1$  as

$$\langle L_{\text{total}} \rangle = \sum_k \langle L^k \rangle = \frac{3}{2}[\langle L_x \rangle - \langle L_y \rangle] \cos(\gamma + \mu_k - 2\alpha_k). \quad (9)$$

Importantly, the obtained quantity is given by the anisotropy in the atomic orbital moment and not by the orbital moment itself.

#### B. Magnetic dipole term

A second sum rule relates the effective spin moment  $\langle S_{\text{eff},\zeta} \rangle$  along the  $\zeta$  direction of a  $3d$  metal to the energy-integrated XMCD intensity over the  $L_3$  absorption edge minus twice that over the  $L_2$  edge [4,23].  $\langle S_{\text{eff},\zeta} \rangle = \langle S_\zeta \rangle + \frac{7}{2}\langle T_\zeta \rangle$ , where  $\langle T_\zeta \rangle$  is the expectation value of the magnetic dipole term  $\mathbf{T} = \hat{\mathbf{S}} - 3\hat{\mathbf{r}}(\hat{\mathbf{r}} \cdot \mathbf{S})$ , with  $\hat{\mathbf{r}}$  the position unit vector [4]. While the spin moment  $\mathbf{S}$  is isotropic,  $\mathbf{T}$  gives the anisotropy of the spin moment due to the coupling with the charge quadrupole moment and spin-flip terms. In agreement with Eq. (39) of Ref. [20],  $\langle T \rangle$  has the same angular dependence as the anisotropic orbital moment, so that for  $h = -1$ ,

$$\langle S_{\text{eff}} \rangle = \sum_k \langle S_{\text{eff}}^k \rangle = \frac{21}{4}[\langle T_x \rangle - \langle T_y \rangle] \cos(\gamma + \mu_k - 2\alpha_k), \quad (10)$$

where the isotropic spin moment has dropped out. If  $\mathbf{T}$  is taken as a quadrupole moment along the  $x$  axis, then  $\langle T_y \rangle = -\frac{1}{2}\langle T_x \rangle$ .

It should be stressed that, contrary to an earlier proposition [6], the presence of  $\mathbf{T}$  is not the unique origin of a nonzero total XMCD for negative chirality structures (see also Sec. I). The sum rule measures  $\langle T \rangle$  in the initial state and this can be zero, such as for the Hund's rule ground state of Mn  $3d^5$ . The anisotropy in the XMCD is then caused by the extra  $d$  electron in the final state. For instance, anisotropic spectra for an isotropic ground state have been reported for Ti  $3d^0 \rightarrow 2p^5 3d^1$  [24].

### IV. CONCLUSIONS

It is shown most generally using a straightforward analytical derivation as well as by graphical illustration that a triangular structure with negative spin chirality allows the existence of a nonzero total XMCD, despite the fact that the total

spin moment vanishes. A necessary condition is an anisotropic XMCD signal ( $I_x \neq I_y$ ) for the local atom.

The nonzero XMCD for negative spin chirality can be understood in a simple way: The anisotropic part of the XMCD signal depends on the angle  $(2\alpha_k - \mu_k)$  with respect to the incident beam direction. This angle is invariant ( $\pm 360^\circ$ ) for a threefold rotation in which  $\alpha_k$  and  $\mu_k$  are rotated by  $120^\circ$  and  $-120^\circ$ , respectively (see Fig. 2 for the angle description). This only holds for threefold symmetric lattices, and a zero value is returned for any other  $n$ -fold symmetry.

The extrema of the total dichroism are found at  $\gamma = 2\alpha_0 - \mu_0$  and  $2\alpha_0 - \mu_0 + 180^\circ$ . Thus, for  $\alpha_0 \neq 0$  the maximum dichroism is not aligned along the spin direction, but also depends on the relative orientation with respect to the atomic orientation. This also implies that if in the experimental setup we do not know  $\alpha_0$ , then a particular spin direction has no unique angular dependence.

By the x-ray magneto-optical sum rules, the orbital and spin moments are proportional to the integrated intensities of the XMCD. Because the total XMCD of the threefold lattice is related to the anisotropic XMCD of the single atom, the integrated intensities yield the anisotropic part of the orbital and effective spin moment, which correspond to  $\langle L_x \rangle - \langle L_y \rangle$  and the magnetic dipole term, respectively. Both display the same angular dependence as the total XMCD. Note that even when the energy-integrated XMCD is zero, the XMCD signal can still be positive and negative in equal amounts across the photon energy range of the absorption edge. Therefore, the presence of an anisotropic orbital moment or a magnetic dipole term is not conditional for a nonzero XMCD signal. For instance, in the x-ray transition  $3d^5 \rightarrow 2p^5 3d^6$  the final state can induce an anisotropy in the XMCD spectrum, while the orbital moment and magnetic dipole term in the Hund's rule ground state  $3d^5$  are zero.

While the presented results confirm earlier cluster calculations [8] and SPR-KKR calculations [9] in fixed geometries, here we developed a general rule under which this effect occurs without the need for any detailed spectral calculations. Importantly, we showed that the effect exists in a coplanar geometry and that noncoplanar spin moments are not required for its existence.

We have not discussed the situation in three dimensions, in which case Eq. (1) also contains a term  $I_z(\hat{\mathbf{P}} \cdot \hat{\mathbf{z}})(\hat{\mathbf{z}} \cdot \hat{\mathbf{S}})$ . If the spin  $\mathbf{S}$  of each atom is in plane, then this term is zero, and for the other terms we can simply take the in-plane components of  $\mathbf{P}$ . If  $\mathbf{S}$  also has an out-of-plane component, then there are three fundamental spectra, which makes an analytical analysis more cumbersome, and beyond the scope of the paper. A numerical calculation would then be more appropriate. Experimentally, one might be able to perform measurements with  $\hat{\mathbf{P}}$  at different angles of incidence, especially  $\mathbf{P} \parallel \mathbf{z}$ , to determine the XMCD contribution from the spin component along the  $z$  direction.

Our findings are useful because antiferromagnets have unique attributes that are not found in ferromagnets, such as high-frequency dynamics, robustness against external perturbations, and absence of stray field, giving rise to new patterns of antiferromagnetic spintronics [25,26] and topological antiferromagnetic spintronics [12].

TABLE I. Irreps for the AFM spin structures shown in Fig. 3 with the three basis vectors  $S_k = (\cos \mu_k, \sin \mu_k)$ , which are the spins in counterclockwise order located on the red, blue, and green atoms, respectively.

Figure	$h$	$\mu_0$	Irreps	$S_0$	$S_1$	$S_2$
3(a)	+1	0°	$S_\perp(A_2)$	(1,0)	$(-\frac{1}{2}, \frac{1}{2}\sqrt{3})$	$(-\frac{1}{2}, -\frac{1}{2}\sqrt{3})$
3(c)	+1	90°	$S(A_1)$	(0,1)	$(-\frac{1}{2}\sqrt{3}, -\frac{1}{2})$	$(\frac{1}{2}\sqrt{3}, -\frac{1}{2})$
3(d)	-1	0°	$S_{2,AF}(E)$	(1,0)	$(-\frac{1}{2}, -\frac{1}{2}\sqrt{3})$	$(-\frac{1}{2}, \frac{1}{2}\sqrt{3})$
3(f)	-1	90°	$S_{1,AF}(E)$	(0,1)	$(\frac{1}{2}\sqrt{3}, -\frac{1}{2})$	$(-\frac{1}{2}\sqrt{3}, -\frac{1}{2})$

### APPENDIX: SPIN CONFIGURATIONS ON TRIANGLE

The AFM spin structures in Fig. 3 are subjected to the point group symmetry  $C_{3v}$ , and their irreps and basis vectors

TABLE II. Character table for the point group symmetry  $C_{3v}$ , with the conjugacy classes under the  $e$  identity operator,  $C_3$  rotations, and  $\sigma_v$  reflections. The irreps  $A_1$ ,  $A_2$ , and  $E$  are in Mulliken notation.

$C_{3v}$	$e$	$C_3$	$\sigma_v$
$A_1$	1	1	1
$A_2$	1	1	-1
$E$	2	-1	0

are given in Table I. The labeling follows the notation in Refs. [27,28]. The character table for the group  $C_{3v}$  is given in Table II. Note that the spin is an axial vector. Kramers theorem tells that by time reversal each triangular structure can also have all its spins reversed. For negative helicity the two irreps  $E$  share the same symmetry properties and can be mixed.

- [1] G. van der Laan and A. I. Figueroa, X-ray magnetic circular dichroism—a versatile tool to study magnetism, *Coord. Chem. Rev.* **277–278**, 95 (2014).
- [2] G. van der Laan and B. T. Thole, Strong magnetic x-ray dichroism in  $2p$  absorption spectra of  $3d$  transition-metal ions, *Phys. Rev. B* **43**, 13401 (1991).
- [3] B. T. Thole, P. Carra, F. Sette, and G. van der Laan, X-Ray Circular Dichroism as a Probe of Orbital Magnetization, *Phys. Rev. Lett.* **68**, 1943 (1992).
- [4] P. Carra, B. T. Thole, M. Altarelli, and X. Wang, X-Ray Circular Dichroism and Local Magnetic Fields, *Phys. Rev. Lett.* **70**, 694 (1993).
- [5] J. Stöhr and H. C. Siegmann, *Magnetism. From Fundamentals to Nanoscale Dynamics* (Springer, Berlin, 2016).
- [6] Y. Yamasaki, H. Nakao, and T. Arima, Augmented magnetic octupole in kagomé 120-degree antiferromagnets detectable via x-ray magnetic circular dichroism, *J. Phys. Soc. Jpn.* **89**, 083703 (2020).
- [7] G. van der Laan, Microscopic origin of magnetocrystalline anisotropy in transition metal thin films, *J. Phys.: Condens. Matter* **10**, 3239 (1998).
- [8] N. Sasabe, M. Kimata, and T. Nakamura, Presence of X-Ray Magnetic Circular Dichroism Signal for Zero-Magnetization State in Antiferromagnetic State, *Phys. Rev. Lett.* **126**, 157402 (2021).
- [9] S. Wimmer, S. Mankovsky, J. Minár, A. N. Yaresko, and H. Ebert, Magneto-optic and transverse-transport properties of noncollinear antiferromagnets, *Phys. Rev. B* **100**, 214429 (2019).
- [10] S. Wimmer, S. Mankovsky, and H. Ebert, Chirality-induced linear response properties in noncoplanar  $Mn_3Ge$ , *Phys. Rev. B* **103**, 024437 (2021).
- [11] M. dos Santos Dias, J. Bouaziz, M. Bouhassoune, S. Blügel, and S. Lounis, Chirality-driven orbital magnetic moments as a new probe for topological magnetic structures, *Nat. Commun.* **7**, 13613 (2016).
- [12] L. Šmejkal, Y. Mokrousov, B. Yan, and A. H. MacDonald, Topological antiferromagnetic spintronics, *Nat. Phys.* **14**, 242 (2018).
- [13] J. Ye, Y. B. Kim, A. J. Millis, B. I. Shraiman, P. Majumdar, and Z. Tesanovic, Berry Phase Theory of the Anomalous Hall Effect: Application to Colossal Magnetoresistance Manganites, *Phys. Rev. Lett.* **83**, 3737 (1999).
- [14] G. Tatara and H. Kawamura, Chirality-driven anomalous Hall effect in weak coupling regime, *J. Phys. Soc. Jpn.* **71**, 2613 (2002).
- [15] M. Taillefumier, B. Canals, C. Lacroix, V. K. Dugaev, and P. Bruno, Anomalous Hall effect due to spin chirality in the Kagomé lattice, *Phys. Rev. B* **74**, 085105 (2006).
- [16] H. Chen, Q. Niu, and A. H. MacDonald, Anomalous Hall Effect Arising from Noncollinear Antiferromagnetism, *Phys. Rev. Lett.* **112**, 017205 (2014).
- [17] P. J. Brown, V. Nunez, F. Tasset, J. B. Forsyth, and P. Radhakrishna, Determination of the magnetic structure of  $Mn_3Sn$  using generalized neutron polarization analysis, *J. Phys.: Condens. Matter* **2**, 9409 (1990).
- [18] S. Nakatsuji, N. Kiyohara, and T. Higo, Large anomalous Hall effect in a non-collinear antiferromagnet at room temperature, *Nature (London)* **527**, 212 (2015).
- [19] T. Higo, H. Man, D. B. Gopman, L. Wu, T. Koretsune, O. M. van 't Erve, Y. P. Kabanov, D. Rees, Y. Li, M.-T. Suzuki, S. Patankar, M. Ikhlas, C. L. Chien, R. Arita, R. D. Shull, J. Orenstein, and S. Nakatsuji, Large magneto-optical Kerr effect and imaging of magnetic octupole domains in an antiferromagnetic metal, *Nat. Photonics* **12**, 73 (2018).
- [20] G. van der Laan, Relation between the angular dependence of magnetic x-ray dichroism and anisotropy of ground state moments, *Phys. Rev. B* **57**, 5250 (1998).
- [21] G. van der Laan, R. V. Chopdekar, Y. Suzuki, and E. Arenholz, Strain-Induced Changes in the Electronic Structure of  $MnCr_2O_4$  Thin Films Probed by X-Ray Magnetic Circular Dichroism, *Phys. Rev. Lett.* **105**, 067405 (2010).
- [22] S. L. Zhang, G. van der Laan, and T. Hesjedal, Direct experimental determination of spiral spin structures via the dichroism extinction effect in resonant elastic soft x-ray scattering, *Phys. Rev. B* **96**, 094401 (2017).

- [23] G. van der Laan, Angular momentum sum rules for x-ray absorption, *Phys. Rev. B* **57**, 112 (1998).
- [24] E. Arenholz, G. van der Laan, A. Fraile-Rodriguez, P. Yu, Q. He, and R. Ramesh, Probing ferroelectricity in  $\text{PbZr}_{0.2}\text{Ti}_{0.8}\text{O}_3$  with polarized soft x-rays, *Phys. Rev. B* **82**, 140103(R) (2010).
- [25] V. Baltz, A. Manchon, M. Tsoi, T. Moriyama, T. Ono, and Y. Tserkovnyak, Antiferromagnetic spintronics, *Rev. Mod. Phys.* **90**, 015005 (2018).
- [26] S. A. Siddiqui, J. Sklenar, K. Kang, M. J. Gilbert, A. Schleife, N. Mason, and A. Hoffmann, Metallic antiferromagnets, *J. Appl. Phys.* **128**, 040904 (2020).
- [27] K. Essafi, O. Benton, and L. D. C. Jaubert, Generic nearest-neighbor kagome model: XYZ and Dzyaloshinskii-Moriya couplings with comparison to the pyrochlore-lattice case, *Phys. Rev. B* **96**, 205126 (2017).
- [28] O. Benton, Ordered ground states of kagome magnets with generic exchange anisotropy, *Phys. Rev. B* **103**, 174425 (2021).